POLITECNICO DI TORINO
Repository ISTITUZIONALE

On the Benefits of Torque Vectoring for Automated Collision Avoidance at the Limits of Handling

Original
On the Benefits of Torque Vectoring for Automated Collision Avoidance at the Limits of Handling / Bertipaglia, A., Tavernini, D., Montanaro, U., Alirezaei, M., Happee, R., Sorniotti, A., Shyrokau, B.. - In: IEEE TRANSACTIONS ON VEHICULAR TECHNOLOGY. - ISSN 0018-9545. - 74:6(2025), pp. 8756-8771. [10.1109/tvt.2025.3538955]

Availability:
This version is available at: 11583/3003036 since: 2025-09-14T19:54:35Z

Publisher:
Institute of Electrical and Electronics Engineers

Published
DOI:10.1109/tvt.2025.3538955

Terms of use:

This article is made available under terms and conditions as specified in the corresponding bibliographic description in the repository

Publisher copyright

(Article begins on next page)

09 November 2026

On the Benefits of Torque Vectoring for Automated Collision Avoidance at the Limits of Handling

Alberto Bertipaglia, *Graduate Student Member, IEEE*, Davide Tavernini, Umberto Montanaro, Mohsen Alirezaei, Riender Happee, Aldo Sorniotti, *Member, IEEE*, and Barys Shyrokau

***Abstract*—This paper presents a novel approach integrating motion replanning, path tracking and vehicle stability for collision avoidance using nonlinear Model Predictive Contouring Control. Employing torque vectoring capabilities, the proposed controller is able to stabilise the vehicle in evasive manoeuvres at the limit of handling. A nonlinear double-track vehicle model, together with an extended Fiala tyre model, is used to capture the nonlinear coupled longitudinal and lateral dynamics. The optimised control inputs are the steering angle and the four longitudinal wheel forces to minimise the tracking error in safe situations and maximise the vehicle-to-obstacle distance in emergency manoeuvres. These optimised longitudinal forces generate an additional direct yaw moment, enhancing the vehicle's lateral agility and aiding in obstacle avoidance and stability maintenance. The longitudinal tyre forces are constrained using the tyre friction cycle. The proposed controller has been tested on rapid prototyping hardware to prove real-time capability. In a high-fidelity simulation environment validated with experimental data, our proposed approach successfully avoids obstacles and maintains vehicle stability. It outperforms two baseline controllers: one without torque vectoring and another one without collision avoidance prioritisation. Furthermore, we demonstrate the robustness of the proposed approach to vehicle parameter variations, road friction, perception, and localisation errors. The influence of each variation is statistically assessed to evaluate its impact on the performance, providing guidelines for future controller design.**

***Index Terms*—Model predictive contouring control, obstacle avoidance, handling limits, torque vectoring, path tracking.**

Received 8 August 2024; revised 11 December 2024 and 21 January 2025; accepted 2 February 2025. Date of publication 6 February 2025; date of current version 20 June 2025. This work was supported in part by Dutch Science Foundation NWO-TTW through EVOLVE project under Grant Nr. 18484,and in part by European Union's Horizon 2020 research and innovation programme under the Marie Skłodowska-Curie actions, under Grant Nr. 872907. The review of this article was coordinated by Dr. Chen Lv. *(Corresponding author: Alberto Bertipaglia.)*

Alberto Bertipaglia, Riender Happee, and Barys Shyrokau are with the Department of Cognitive Robotics, Delft University of Technology, 2628 CD Delft, The Netherlands (e-mail: A.Bertipaglia@tudelft.nl; r.happee@tudelft.nl; b.shyrokau@tudelft.nl).

Davide Tavernini and Umberto Montanaro are with the Centre for Automotive Engineering, University of Surrey, GU2 7XH Guildford, U.K. (e-mail: d.tavernini@surrey.ac.uk; u.montanaro@surrey.ac.uk).

Mohsen Alirezaei is with the Department of Mechanical Engineering, University of Eindhoven, 5612 AZ Eindhoven, The Netherlands, and also with the Digital Industry-Software-Simulation and Testing Services, 5708 JZ Helmond, The Netherlands (e-mail: m.alirezaei@tue.nl).

Aldo Sorniotti is with the Departement of Mechanical and Aerospace Engineering, Politecnico di Torino, 10129 Torino, Italy (e-mail: aldo.sorniotti @polito.it).

Digital Object Identifier 10.1109/TVT.2025.3538955

I. Introduction

ENSURING automated vehicles can adeptly avoid obstacles at the limit of handling, which is essential for maximising safety in real-world driving scenarios. Nonetheless, the highly nonlinear characteristics of tyres, mainly when longitudinal and lateral forces interact, present a notable challenge [1], [2]. A prevalent strategy entails developing collision avoidance controllers that optimise steering angle and total longitudinal brake force. However, a pure braking force can potentially lead to dangerous situations. For example, a vehicle must accelerate after performing an evasive manoeuvre to avoid a rear-end collision or quickly steer to the original lane during a double-lane change manoeuvre. Furthermore, purely braking and steering commands may not act fast enough to prevent a collision in an emergency manoeuvre [3]. Thus, we develop a collision avoidance controller which includes a positive acceleration force in addition to the typical inputs such as braking force and steering angle. Moreover, we extend the controller with torque vectoring capabilities to enhance vehicle lateral agility and yaw rate control.

Vehicle obstacle avoidance controllers are typically based on a hierarchical architecture that splits motion planning, path tracking, and vehicle stability objectives into separate controllers. This simplifies the cost function formulation of each layer and allows the adoption of a different prediction model for each controller (Fig. 1(a)). For instance, the motion planner can adopt a simple kinematic model to extend the prediction horizon or include a probabilistic approach to deal with uncertainties [4]. However, the three different objectives might conflict with each other, e.g. the vehicle stability controller introduces an unwanted tracking error to keep the vehicle stable, or the path tracking cannot perfectly track the motion planner trajectory due to the different complexity in the prediction models. Thus, various Model Predictive Control (MPC) algorithms have recently been introduced to integrate motion planning, path tracking and vehicle stability objectives into a single controller for vehicle collision avoidance during emergency manoeuvres [5], [6], [7], [8]. Despite the improved performance of integrated vehicle obstacle avoidance controllers, they have yet to be enabled to utilise torque vectoring capabilities (Fig. 1(b)). Emerging control methodologies incorporating torque vectoring have gained significant appeal in light of the recent development of new electric powertrains, notably those employing multiple in-wheel electric motors [9], [10], [11].

© 2025 The Authors. This work is licensed under a Creative Commons Attribution-NonCommercial-NoDerivatives 4.0 License. For more information, see https://creativecommons.org/licenses/by-nc-nd/4.0/

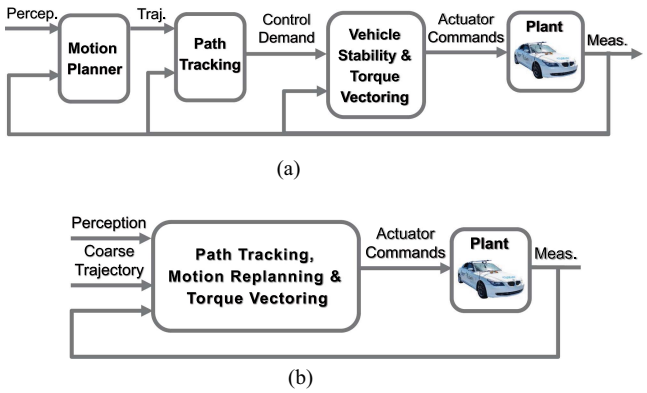

Fig. 1. Hierarchical architecture for vehicle obstacle avoidance (a); proposed architecture (b).

Thus, this paper proposes a vehicle obstacle avoidance approach consisting of Model Predictive Contouring Control (MPCC), which combines motion planning, path tracking, and vehicle stability tasks into a single cost function, prioritising vehicle collision avoidance in case of an emergency. Furthermore, the approach employs torque vectoring capabilities to improve the vehicle's lateral agility at the limit of handling. The torque vectoring is enabled in the optimal control problem formulation thanks to the adoption of a double-track vehicle model based on an extended Fiala tyre model. The proposed tyre model captures the effect of longitudinal force on the cornering stiffness and the diminishing tyre saturation region. This improves the accuracy of the prediction model, reducing the vehicle model mismatch with the plant while maintaining the real-time feasibility on a rapid prototyping platform.

This paper is organised as follows: Section II summarises the previous works and the main paper contributions, highlighting the differences and improvements compared with our previous conference paper [12]. Section III presents the prediction model. Section IV describes the proposed controller. Section V shows the experimental setup, summarising the results in Section VI. Section VII concludes the essential findings and future works.

II. Related Works

A sizeable amount of literature exists on obstacle avoidance controllers. For the sake of brevity, a selection of the most relevant research is presented herein.

One line of research has focused on solutions represented by a three-layer control framework: a Nonlinear Model Predictive Control (NMPC) for path tracking, a stability controller to compute the reference yaw rate, and an optimal tyre force allocation algorithm for torque vectoring [13]. NMPC is based on a single-track formulation with a linear tyre model. Given the significant model mismatch intrinsic in the simplistic tyre model, the stability controller layer calculates a desired steady-state yaw rate to ensure vehicle stability. Meanwhile, the torque vectoring layer optimally distributes tyre forces across each wheel based on the pre-calculated desired yaw rate and longitudinal force. Simulation results showcase enhancements in lateral stability and reductions in path tracking error. However, the limited accuracy of the linear tyre model during emergency manoeuvres significantly reduces performance. Additionally, separating the path tracking layer from the reference yaw rate computation diminishes the advantages of torque vectoring. For instance, even a simple Linear Quadratic Regulator controller with integrated path tracking and torque vectoring achieves a higher entry speed and vehicle agility in a double-lane change than a split controller configuration [14].

An integrated MPC [3] is proposed to address these challenges. The MPC incorporates steering and differential braking strategies to facilitate collision avoidance [3]. The approach splits the longitudinal and lateral dynamics, with the MPC utilising a linearised brush tyre model to calculate the desired lateral tyre force and additional differential braking moment. However, the accuracy of the linearised tyre model diminishes significantly at handling limits and neglects the interaction between longitudinal and lateral dynamics. Moreover, the prediction relies on a single-track vehicle model, limiting the maximum stabilising yaw moment by a portion of the tyre force capacity. This limitation is necessary to safeguard the vehicle's lateral force capacity from unmodeled dynamics, i.e. combined slip and lateral weight transfer, resulting in a more conservative controller approach.

A similar approach relies on a single-track vehicle model to control the steering angle, the braking force distribution and an additional yaw moment [15]. The controller can drive the vehicle at the handling limit and even maintain the vehicle in a drifting equilibrium. Nonetheless, due to the constrained prediction horizon of 1 s necessary for real-time execution and the cost function formulation, there is no possibility for trajectory replanning in emergency scenarios, when obstacles might suddenly change their position unless a new reference trajectory is provided to the path tracking algorithm. A similar limitation is recognisable also for a dynamic inversion-based path tracking controller recently proposed to control the vehicle beyond and within the stability limits [16].

A Model Predictive Contouring Control (MPCC) based on a nonlinear single-track vehicle model has been proposed for vehicle collision avoidance at the limit of handling [5]. By adopting a Cartesian reference frame, the MPCC delineates the vehicle's kinematics, ensuring precise measurement of the vehicle-to-obstacle (V2O) distance, a factor prone to overestimation when employing the Frenet reference frame [6]. Additionally, it circumvents the need for supplementary optimisation to compute the distance travelled by the vehicle to the reference line [5], [17]. Thus, its safety performance is superior to controllers based on hierarchical architecture [7], [18], [19] and even surpasses an integrated architecture reliant on the Frenet reference system [6]. However, the controller does not consider the torque vectoring capabilities, and the single-track vehicle model cannot accurately capture the effect of lateral load transfer on vehicle handling.

This paper extends the design and the analysis of the solution presented in [12], proposing an MPCC controller based on a nonlinear double-track vehicle with an extended Fiala tyre model for collision avoidance at the limit of handling. The approach is extended to consider the torque vectoring capabilities, and

it integrates motion replanning, path tracking, torque vectoring and vehicle stability tasks, prioritising vehicle collision avoidance. The additional complexity brought by the longitudinal tyre force optimisation requires a reduction of the model mismatch, specifically in the tyre. Thus, the Fiala tyre model is extended to accurately reflect the variability of cornering stiffness with vertical and longitudinal forces and adjustments to its saturation region to capture the tyre behaviour in the combined slip conditions. The added complexity allows the MPCC to optimise directly the longitudinal tyre forces and the yaw moment without using a lower controller for force allocation. This reduces architecture conservativeness [20], improving the collision avoidance performance. Despite the controller complexity, the proposed MPCC runs in real-time on a rapid prototyping platform, contrary to our conference paper [12], and is extensively evaluated in a high-fidelity simulation environment validated with experimental data.

The contributions of this paper are threefold. The first is the development of the first real-time feasible MPCC controller augmented with torque vectoring functionalities that can safely avoid vehicle collisions in a double-lane change manoeuvre at the limit of handling. In contrast, existing state-of-the-art approaches [5], [6] would result in a collision under similar conditions or not work in real-time [12]. Leveraging the improved responsiveness induced by torque vectoring, the vehicle is directed away from the obstacle, ensuring stability and preventing potential crashes. Unlike our previous conference paper [12], the first contribution is extended to an analysis of the proposed controller in low friction conditions ($\mu = 0.5$), e.g. in heavy rain. Even in these conditions, the proposed controller can successfully avoid the obstacles without losing stability. Furthermore, it is tested at different initial velocities, highlighting its higher performance in a broader set of initial conditions compared to the baselines.

The second contribution involves applying and rigorously evaluating an extended Fiala tyre model capable of capturing variations in cornering stiffness relative to longitudinal and vertical forces and adjusting the gradient within the tyre's saturation region without losing the continuity of the function. It significantly enhances the accuracy of the prediction model, so its applicability for the controller in scenarios with high levels of force coupling, e.g. when torque vectoring is enabled. Due to the increased accuracy provided by the extended Fiala tyre model, the wheel dynamics can be neglected in the prediction model. This simplification allows for an increased sampling time and reduced computational effort.

In contrast to our conference paper [12], the third contribution is the robustness evaluation of the proposed MPCC with torque vectoring against variations in vehicle and tyre parameters, perception inaccuracies, false negatives, and localisation errors, compared to baseline controllers. Notably, the collision rate of the proposed controller is 31.20 % and 38.50 % for vehicle parameter and perception inaccuracies, respectively, compared to nearly $\sim$ 100 % for the baseline controllers. Additionally, the sensitivity analysis offers numerical insights into which parameters and perception inaccuracies have the most significant impact on the performance degradation of obstacle avoidance MPCC controllers. Specifically, the lateral peak friction coefficient and the obstacle localisation inaccuracies in the lateral direction emerge as the most influential factors affecting controller performance.

III. Prediction Model

This section presents the prediction model implemented in the proposed MPCC controller. At first, the double-track vehicle model is described. Second, the extended Fiala tyre model with the proposed improvements is presented.

A. Double-Track Vehicle Model

The proposed MPCC integrates a nonlinear double-track vehicle model, chosen over the single-track vehicle model [3], [6], [21] due to its ability to capture lateral weight transfer and its superior accuracy at the vehicle's handling limits [2]. However, it is simplified by neglecting roll and pitch dynamics due to their relatively small contribution to load transfer for the considered vehicle class. The prediction model comprises twelve states denoted by $x = [X, Y, \psi, v_x, v_y, r, \theta, \delta, F_{x,fl}, F_{x,fr}, F_{x,rl}, F_{x,rr}]$. These states describe the vehicle's position and orientation in a Cartesian reference system: longitudinal position (X), lateral position (Y), and the heading angle (ψ) of the vehicle's centre of gravity (CoG) relative to an inertial frame. Additionally, longitudinal and lateral velocities at the CoG (v_x and v_y, respectively) and yaw rate (r) are included. The MPCC requires knowing the vehicle's travelled distance (θ), utilised by the cost function to compute the vehicle's position relative to the reference line; thus, θ is incorporated as an extra state [5]. The road wheel angle (δ) and the longitudinal forces at the front left $(F_{x,fl})$, front right $(F_{x,fr})$, rear left $(F_{x,rl})$, and rear right $(F_{x,rr})$ wheels are controlled via their derivatives, leading to five additional equations of motion. The state derivatives are computed as follows:

$$\begin{cases} \dot{X} = v_x \cos(\psi) - v_y \sin(\psi) \\ \dot{Y} = v_x \sin(\psi) + v_y \cos(\psi) \\ \dot{\psi} = r \\ \dot{v}_x = \frac{1}{m}\Big((F_{x,fl} + F_{x,fr}) \cos(\delta) - (F_{y,fl} + F_{y,fr}) \sin(\delta) \\ + F_{x,rl} + F_{x,rr} - F_{res} \Big) + r v_y \\ \dot{v}_y = \frac{1}{m}\Big((F_{x,fl} + F_{x,fr}) \sin(\delta) + (F_{y,fl} + F_{y,fr}) \cos(\delta) \\ + F_{y,rl} + F_{y,rr} \Big) - r v_x \\ \dot{r} = \frac{1}{I_{zz}}\Big((F_{y,fl} + F_{y,fr}) \cos(\delta)\, l_f - (F_{y,rl} + F_{y,rr})\, l_r \\ + (F_{x,fl} + F_{x,fr}) \sin(\delta)\, l_f + \frac{t_f}{2} (F_{y,fl} - F_{y,fr}) \sin(\delta) \\ + \frac{t_f}{2} (F_{x,fr} - F_{x,fl}) \cos(\delta) + \frac{t_r}{2} (F_{x,rr} - F_{x,rl}) \Big) \\ \dot{\theta} = \sqrt{v_x^2 + v_y^2} \end{cases} \tag{1}$$

where $F_{x,ij}$ and $F_{y,ij}$ are the longitudinal and lateral tyre forces, i stands for front (f) or rear (r), and j stands for left

TABLE I
VEHICLE PARAMETERS DESCRIPTION

Parameters	Symbol	Value
Vehicle mass	m	1997 kg
Vehicle inertia around the z-axis	I_{zz}	3198 kgm^2
Distance between the front axle to CoG	l_f	1.430 m
Distance between the rear axle to CoG	l_r	1.455 m
Front axle track width	t_f	1.540 m
Rear axle track width	t_r	1.576 m
Air density	ρ	1.204 kg/m^3
Drag coefficient	C_{d1}	0.25
Rolling resistance	C_{d0}	45 N
Vehicle frontal area	A_f	2.4 m^2

(l) or right (r). All other vehicle parameters are reported in Table I. Moreover, F_{res} is the aerodynamic drag and the rolling resistance computed according to the following equation:

$$F_{res} = \frac{1}{2}\rho A_f C_{d1} v_x^2 + C_{d0} \tag{2}$$

The vehicle model inputs are the rates of the previously mentioned road wheel angle and the rates of longitudinal forces applied to each wheel, i.e. $(u_v = [\dot{\delta}, \dot{F}_{x,fl}, \dot{F}_{x,fr}, \dot{F}_{x,rl}, \dot{F}_{x,rr}])$. The rates are used as inputs to apply constraints representing actuator dynamics and create further responses. The decision to use longitudinal forces as inputs, rather than motor torques or longitudinal slips, simplifies the vehicle model by eliminating the need to account for wheel or motor dynamics in the MPC prediction model. This not only reduces computational complexity but also facilitates the implementation of constraints, allowing tyre forces to be constrained using the tyre friction circle [6], [22].

The vehicle and obstacles are represented as circles so the MPCC controller can constantly monitor the V2O distance. A similar approach is implemented for the vehicle-to-edge (V2E) of the road distance. Their Euclidean distance is computed as follows:

$$D_{V2O} = \sqrt{(X - X_{obs})^2 + (Y - Y_{obs})^2} - r_{obs} - r_{veh} \tag{3}$$

where X, Y and X_{obs}, Y_{obs} are, respectively, the longitudinal and lateral position of the vehicle and obstacle centre, and r_{veh} and r_{obs} are the radii of the vehicle and obstacle circles. The proposed MPCC controller aims to keep D_{V2O} above a user-defined safety distance. The vehicle and the obstacles will collide if D_{V2O} is lower than zero.

B. Extended Fiala Tyre Model

The lateral tyre forces for each wheel of the double-track vehicle model are captured by an extended Fiala tyre model. The classic Fiala tyre model is modified to capture the variation of cornering stiffness depending on the longitudinal and vertical force [2], and the saturation region is adapted to include a negative gradient. The latter allows the prediction model not to overestimate the maximum lateral force when the tyre works with a high lateral slip angle, e.g. driving at the limit of handling or drifting. The extended Fiala tyre model is defined as follows:

$$F_y(\alpha, F_x, F_z) = \begin{cases} -C_{ym}(F_x, F_z)\tan\alpha + \frac{C_{ym}^2(F_x,F_z)\tan\alpha\tan|\alpha|}{3F_{y,\max}} \\ -\frac{C_{ym}^3(F_x,F_z)\tan\alpha^3}{27F_{y,\max}^2}, & |\alpha| \le \alpha_{thr} \\ \frac{2C_{ym}(F_x,F_z)(\zeta-1)\tan\alpha}{3} - \frac{C_{ym}^2(F_x,F_z)(\zeta-1)\tan\alpha|\tan\alpha|}{9F_{y,\max}} \\ -F_{y,\max}\zeta\,\mathrm{sign}(\alpha), & |\alpha| > \alpha_{thr} \end{cases} \tag{4}$$

where α is the tyre slip angle, C_y is the tyre cornering stiffness, which is a function of the vertical (F_z) and longitudinal (F_x) tyre force, $F_{y,\max}$ is the maximum lateral tyre force, α_{thr} is the tyre slip threshold corresponding to the peak of the tyre lateral force, and ζ is a parameter defined between 0 and 2 which characterises the gradient of the saturation region. When $\alpha \le \alpha_{thr}$, apart from the effect of F_x, which is also active for low lateral slip, the extended Fiala model is formulated as the classic Fiala tyre model [23], while the saturated region $(\alpha > \alpha_{thr})$ is modified to have a gradient that better captures the maximum lateral force reduction with large slip angles. At the same time, the proposed model still keeps the advantages of the classical Fiala tyre, so it is fully continuous and differentiable when $\alpha = \alpha_{thr}$. A gradient different from zero in the saturation region helps numerical optimisation algorithms based on the gradient calculation to avoid derivative vanishing and to optimise the road wheel angle when the tyre works in the saturation region [24]. Furthermore, the proposed solution has a positive gradient when $\zeta \in [1, 2]$ and a negative one when $\zeta \in [0, 1]$.

To further reduce the tyre model mismatch, the C_y is not considered constant, but it is firstly adapted depending on the vertical force [2] as follows:

$$C_y(F_z) = c_1 F_{z0} \sin\left(2\,\mathrm{atan}\left(\frac{F_z}{c_2 F_{z0}}\right)\right) \tag{5}$$

where c_1 and c_2 are tunable parameters, and F_{z0} is the nominal vertical load. Second, the tyre model considers the coupling effect between longitudinal and lateral axle forces, so the previously computed C_y is further modified to capture the F_x dependency in accordance with literature [2], [25] as follows:

$$C_{ym}(F_x, F_z) = \frac{1}{2}(\mu F_z - F_x) + \left(1 - \left(\frac{|F_x|}{\mu F_z}\right)^{c_3}\right)^{1/c_3}\left(C_y(F_z) - \frac{1}{2}\mu F_z\right) \tag{6}$$

where c_3 is a user-defined parameter, which is in the range of 2 to 8 [25], and μ is the friction coefficient. The $C_{ym}(F_x, F_z)$ is used to compute the tyre slip threshold (α_{thr}) as follows:

$$\alpha_{thr} = \frac{3F_{y,\max}}{C_{ym}(F_x, F_z)} \tag{7}$$

The maximum lateral tyre force $(F_{y,\max})$ is limited by the tyre friction circle, defined as follows:

$$F_{y,\max} = \sqrt{(\mu F_z)^2 - F_x^2} \tag{8}$$

TABLE II
TYRE PARAMETERS DESCRIPTION

Parameters	Symbol	Value
Lateral cornering stiffness effect	c_1	49.3
Lateral cornering stiffness peak effect	c_2	3.5
Long. and Lat. tyre force coupling effect	c_3	4.1
Saturation region gradient	ζ	0.87
Nominal vertical tyre force (as in .tir property file)	F_{z0}	4300 N
Tyre friction coefficient	μ	0.95

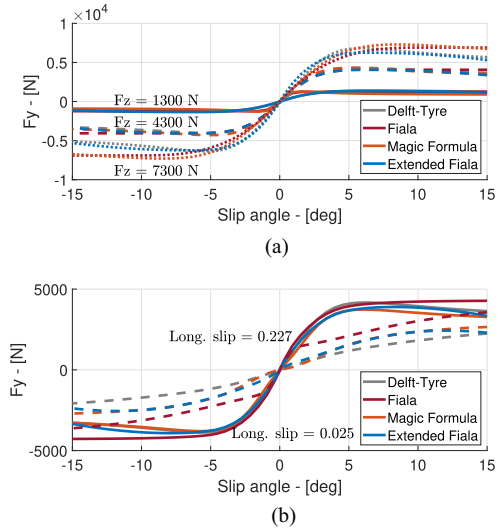

Fig. 2. Lateral force of the high-fidelity Delft tyre model, the classic Fiala, the simplified Magic Formula and the extended (proposed) Fiala tyre model for pure slip conditions (a); lateral forces of the models in the combined slip conditions (b).

All the parameters used in the extended Fiala tyre model are reported in Table II, and their value is obtained by performing a nonlinear optimisation known as Two-Stage Bayesian Optimisation [26]. The parametrisation process involves two steps: first, the tyre models are optimised to minimise discrepancies in lateral forces compared to a high-fidelity Delft-Tyre 6.2 model, using nominal loads from 1000 N to 8000 N representative of double lane change manoeuvres at the limit of handling. Second, the tyre parameters are further optimised against experimental data from skidpad manoeuvres in clockwise and counterclockwise directions. Notably, the optimisation and evaluation manoeuvres differ to avoid overfitting and ensure robust model validation. Fig. 2 shows how the proposed extended Fiala tyre model captures the effect of the normal load on the tyre cornering stiffness and how the model mismatch between the Delft tyre model and the proposed one is reduced not only in the linear region but also around the peak lateral force area. Particularly relevant is the saturated region, which is well matched by the extended Fiala tyre model while it is overestimated by the classic Fiala tyre model with a constant saturation region [2], [6], [23] or by the simplified Magic Formula when subjected to an increased vertical force of 7300 N. A model mismatch in the tyre's large slip angle working area is particularly detrimental for obstacle avoidance controllers at the limit of handling. Fig. 2 shows that the cornering stiffness of the proposed extended Fiala model captures the longitudinal and lateral force coupling more accurately, which is important for the scope of this work. The

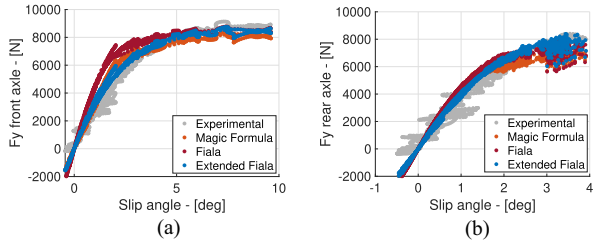

Fig. 3. Front (a) and rear (b) lateral forces for the classic Fiala, the simplified Magic Formula, the extended (proposed) Fiala tyre model and experimental measurements in a quasi-steady-state circular driving test.

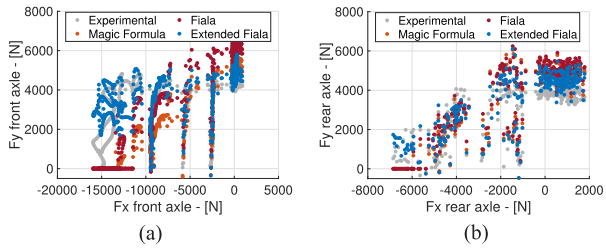

Fig. 4. Front (a) and rear (b) lateral forces for the classic Fiala, the simplified Magic Formula, the extended (proposed) Fiala tyre model and experimental measurements in four braking-in-a-turn manoeuvrers with different longitudinal accelerations.

reason is that the proposed MPCC uses torque vectoring capabilities, which implies using a longitudinal force coupled with a lateral one. Furthermore, the optimised tyre model is experimentally validated by performing a quasi-steady-state circular driving test and four braking in a turn manoeuvrers with different longitudinal accelerations ranging from a minimum of $-1.5\,\mathrm{m/s^2}$ to a maximum of $-8.5\,\mathrm{m/s^2}$. Fig. 3 shows how the extended Fiala tyre model captures the linear and nonlinear tyre working regions, slightly outperforming the simplified Magic Formula in these conditions. Furthermore, the proposed extended Fiala tyre model outperforms both the classic Fiala and simplified Magic Formula models in four experimentally recorded braking-in-turn manoeuvrers, as shown in Fig. 4. It is particularly noteworthy that as the longitudinal force increases, the model mismatch between experimental data and both the classic Fiala and simplified Magic Formula becomes more pronounced, whereas the extended Fiala tyre model continues to maintain its accuracy.

IV. MODEL PREDICTIVE CONTOURING CONTROL USING TORQUE VECTORING

This section explains how the cost function and the constraints of the proposed MPCC are formulated. Section IV-A focuses on describing the MPCC cost function and how it is designed to prioritise obstacle avoidance over path tracking in case of emergency. Section IV-B explains how the MPCC constraints are defined to improve safety, taking into account the vehicle actuators' limitations, and avoid redundant torque vectoring utilisation.

A. Cost Function With Obstacle Avoidance Prioritisation

The proposed MPCC is based on iterative optimisation of a nonlinear cost function ($J = J_{track} + J_{inp} + J_{obs}$) [5], which is responsible for ensuring path tracking (J_{track}), minimising

the control effort (J_{inp}) and obstacle avoidance prioritisation (J_{obs}) in case of emergency.

The path tracking properties in the cost function are defined as follows:

$$J_{track} = \sum_{i=1}^{N} \left(q_{e_{Con}} e_{Con,i}^2 + q_{e_{Lag}} e_{Lag,i}^2 + q_{e_{Vel}} e_{Vel}^2 \right) \quad (9)$$

where N is the length of the prediction horizon, e_{Con} is the contouring error, e_{Lag} is the lag error, e_{Vel} is the velocity error and q_* are the weights of the respective quadratic errors. The path is followed by minimising the contouring (e_{Con}) and the lag error (e_{Lag}) [5], [17]. e_{Con} represents the vehicle position projection onto the desired trajectory, depending on the vehicle's travelled distance related to the reference line (θ_s). However, contrary to MPC or NMPC controllers [1] based on a Frenet reference system, θ_s is unavailable for an MPCC based on a Cartesian reference frame. Thus, θ_s is approximated by the vehicle total travelled distance (θ), and the approximation accuracy is ensured by the lag error minimisation, defined as the norm between the two distances. Mathematically, e_{Con} and e_{Lag} are defined as follows:

$$\begin{aligned} e_{Con} &= \sin\left(\Psi_t\left(\theta\right)\right)\left(X - X_t\left(\theta\right)\right) - \cos\left(\Psi_t\left(\theta\right)\right)\left(Y - Y_t\left(\theta\right)\right) \\ e_{Lag} &= -\cos\left(\Psi_t\left(\theta\right)\right)\left(X - X_t\left(\theta\right)\right) - \sin\left(\Psi_t\left(\theta\right)\right)\left(Y - Y_t\left(\theta\right)\right) \end{aligned} \quad (10)$$

X_t, Y_t, and Ψ_t are the desired longitudinal and lateral positions and heading angle. Despite the added nonlinearities and complexities of e_{Con} and e_{Lag}, they allow an approximation of the Frenet reference frame with a Cartesian reference frame, which means that V2O distance is never overestimated [5]. The MPCC based on a Cartesian frame is more pre-emptive than an NMPC based on a Frenet reference frame in prioritising collision avoidance over path tracking [5]. Thus, the vehicle is more prone to stay inside a safe and stable working area even when it needs to avoid a collision at the limit of handling. Furthermore, the e_{Lag} is equal to zero only when the vehicle follows the reference trajectory perfectly. As soon as the desired velocity is unfeasible for the planned trajectory, the MPCC will modify the desired velocity to minimise the e_{Lag}. The reference velocity is tracked by minimising the quadratic error between the vehicle velocity (v_x) and the desired one (v_{des}). For what concerns the weights, they are firstly empirically tuned to reduce the path tracking error and the vehicle sideslip angle peaks [27], [28]. Second, they are fine-tuned using a two-stage Bayesian optimisation [26]. It is important to highlight that $q_{e_{Vel}}$ is tuned to have a low weight in magnitude because the controller must allow the vehicle to slow down in case of obstacle avoidance prioritisation [5], [6].

The minimisation of the control inputs is ensured in the cost function as follows:

$$\begin{aligned} J_{inp} = \sum_{i=1}^{N} \Big(& q_{\dot{\delta}} \dot{\delta}_i^{\,2} + q_{\dot{F}_x} \dot{F}_{x,FL,i}^2 + q_{\dot{F}_x} \dot{F}_{x,FR,i}^2 \\ & + q_{\dot{F}_x} \dot{F}_{x,RL,i}^2 + q_{\dot{F}_x} \dot{F}_{x,RR,i}^2 \Big) \end{aligned} \quad (11)$$

TABLE III
UPPER AND LOWER CONSTRAINTS [1], [5], WHERE i STANDS FOR FRONT OR REAR, AND j FOR LEFT OR RIGHT

Symbol	Boundaries	Symbol	Boundaries
$\dot{\delta}$	± 90 deg/s	δ	± 18 deg
$\dot{F}_{x,ij}$	± 7200 N/s	$F_{x,ij}$	± 3600 N

where $\dot{\delta}$ is the road wheel angle rate, and $\dot{F}_{x,FL}$, $\dot{F}_{x,FR}$, $\dot{F}_{x,RR}$, and $\dot{F}_{x,RR}$ are the rate of the longitudinal forces applied to each of the vehicle's four wheels. These cost terms are added in order to make the control inputs smooth, and they are considered equal to simplify the tuning.

The motion replanning for obstacle avoidance prioritisation is defined as follows:

$$J_{obs} = \sum_{i=1}^{N} \left(\sum_{j=1}^{N_{obs}} \left(q_{e_{V2O}} e_{V2O,j,i}^2 \right) + \sum_{j=1}^{N_{edg}} \left(q_{e_{V2E}} e_{V2E,j,i}^2 \right) \right) \quad (12)$$

where N_{obs} and N_{edg} are the number of obstacles and road edges, e_{V2O} and e_{V2E} are the difference between the V2O and V2E distances and the user defined safety distances between the obstacles $(D_{Sft,O})$ and the road edges $(D_{Sft,E})$. When the vehicle is at a safe distance from obstacles or road edges, it does not interfere with the path tracking properties of the MPCC. On the other hand, the e_{V2O} and e_{V2E} errors allow the MPCC controller to dynamically perform a short trajectory replanning when the vehicle passes close to the obstacles. The obstacle avoidance prioritisation is due to the dynamically varying weights associated with e_{V2O} and e_{V2E} [5]. The weights, here reported only q_{V2O} for compactness, vary as follows:

$$q_{V2O} = \begin{cases} P_k, & \text{if } D_{V2O} < 0 \\ P_k \, e^{-\frac{2D_{V2O}^2}{D_{Sft,O}^2}}, & \text{elseif } 0 \le D_{V2O} \le D_{Sft,O} \\ 0, & \text{otherwise} \end{cases} \quad (13)$$

where P_k denotes the upper limit of the achievable value for q_{V2O}. The magnitude of q_{V2O} increases with a Gaussian-shaped curve with the decrease of the V2O distance, and it is zero when V2O is above $D_{Sft,O}$.

B. Constraints

The constraints are designed to accommodate actuator limitations, vehicle stability, and path tracking and to avoid redundant torque vectoring utilisation. The actuators' limitations are applied to δ, $F_{x,FL}$, $F_{x,FR}$, $F_{x,RR}$, and $F_{x,RR}$ and their respective rates. The values implemented are reported in Table III.

The vehicle stability is enforced using the tyre friction circle, as described in the extended Fiala tyre model, and as follows [5], [6]:

$$F_{x,ij} \le S_f \mu F_{z,ij} \quad (14)$$

where S_f is a safety factor that limits the applicable longitudinal force considering the tyre road friction coefficient uncertainty

(μ), and the subscripts ij represent the front-rear axle and left-right side.

The following inequality forces the vehicle to stay inside the road boundaries:

$$\left\| \begin{bmatrix} X \\ Y \end{bmatrix} - \begin{bmatrix} X_{cen} \\ Y_{cen} \end{bmatrix} \right\|^2 \leq \left(\frac{W_t}{2} \right)^2 \tag{15}$$

where X_{cen} and Y_{cen} are the longitudinal and lateral locations of the track's centre, and W_t is the road width [17].

The MPCC is constrained not to use redundant torque vectoring while driving in a straight to avoid excessive tyre wear and energy consumption as follows:

$$\begin{aligned} |F_{x,FL} - F_{x,FR}| &\leq |F_{z,FL} - F_{z,FR}| T_s \\ |F_{x,RL} - F_{x,RR}| &\leq |F_{z,RL} - F_{z,RR}| T_s \end{aligned} \tag{16}$$

where T_s is a user-defined parameter which works as a safety coefficient, allowing a difference in the longitudinal forces higher than the normal load difference between the right and left sides of the vehicle.

V. Simulation Setup and Experimental Validation

This section is split into three subsections. Section V-A describes how the proposed MPCC is implemented in a real-time rapid prototyping platform and how it is assessed in high and low friction conditions. Section V-B explains how the high-fidelity and prediction models are validated using experimental data. Section V-C presents how the MPCC robustness is evaluated and how the controller sensitivity to vehicle parameter variations and perception inaccuracies is computed.

A. Hard Real-Time Implementation and Simulation Setup

The proposed MPCC is tested using the dSPACE SCALEXIO real-time platform, which operates on a multi-core DS6001 processor (2.8 GHz quad-core, 1 GB DDR2 SD RAM). In this setup, the MPCC is allocated to a distinct core separate from the vehicle plant. The prediction model is discretised using the Runge-Kutta 2 method, chosen for its balanced trade-off between computational effort and accuracy [6]. A control integration interval of 0.05 s is used, with 10 integrator nodes and a prediction horizon of 30 steps to ensure the real-time feasibility of the controller implementation. The optimisation problem is solved using the nonlinear interior-point solver available in FORCESPro [29], with the Hessian matrix approximation based on the Broyden–Fletcher–Goldfarb–Shanno (BFGS) algorithm. Rather than initializing the Hessian with an identity matrix, an efficient initial estimate is employed by averaging optimised BFGS matrices from multiple manoeuvrers, reducing computational effort without compromising performance. To further decrease computational time, especially on embedded platforms, the variational derivative method is utilised for differentiation method instead of the conventional chain rule [29]. The maximum number of iterations is set to 100 as extensive testing revealed that the solver consistently finds an optimal solution within this limit. The platform demonstrates effective execution of the nonlinear optimisation, achieving an average solving time of 38.9 ms, with minimum and maximum solving times of 30.7 ms and 41.8 ms, respectively. The computational solving time corresponds to the total time required by dSPACE to compute the parameters, such as the reference trajectory sent to the MPCC, solve the optimization problem, and transmit the optimized control inputs to the vehicle plant. Although the maximum number of iterations is limited to 100 to partially control the solving time, it is important to note that there is no formal guarantee of solver convergence within this predetermined time frame [6]. However, no convergence issues were observed in the performed test. The vehicle plant operates on a separate core at 1000 Hz. It is a high-fidelity representation of a BMW Series 545i vehicle built upon an IPG CarMaker platform, modified to include four in-wheel electric motors. Experimental measurements conducted on a proving ground are used for validation purposes to appropriately select the vehicle parameters. The suspension settings are tuned based on Kinematics & Compliance test rig measurements, while the tyre dynamics are described using the experimentally validated Delft-Tyre 6.2 model. Steering dynamics are accounted for using a second-order transfer function to enhance the fidelity of the vehicle model [30]. The electric motors exhibit faster dynamics than conventional powertrains, and they are modelled with a first-order transfer function and a delay adjusted based on measurements conducted on a powertrain rig provided by the electric motor manufacturer. The electric motor has a time constant of $\sim$ 25 ms, and the initial inverter reaction can be neglected [31], [32]. The control inputs for the MPCC, representing longitudinal forces mapped to the desired torque, are subsequently passed to a low-level control system that tracks these inputs [31], [32]. It is important to highlight that, although the MPCC prediction model does not account for wheel and electric motor dynamics, these dynamics are incorporated in the vehicle plant model. The torque ripple is modelled as a Fourier series as follows [33]:

$$\begin{aligned} T_{rip} = {} & As_1 \sin(p_1 \omega_r) + Ac_1 \cos(p_1 \omega_r) \\ & + As_2 \sin(2p_1 \omega_r) + Ac_2 \cos(2p_1 \omega_r) \end{aligned} \tag{17}$$

where ω_r is the rotor velocity, p_1 is the least common multiple of the electric motor's stator slots and pole numbers, and As_1, As_2, Ac_1, and Ac_2 are coefficients dependent on the electric motor. The torque ripple (T_{rip}) is added to the electric motor torque calculated by a first-order transfer function. Although the influence of torque ripple is minor for vehicle path tracking, mainly due to its effects being filtered by the drivetrain and tyres [33], incorporating torque ripple in the high-fidelity simulation model can reveal discrepancies under different load conditions or varying speed scenarios.

The proposed MPCC controller with torque vectoring and collision avoidance properties (MPCC TV+CA) is compared with two baselines:

- MPCC CA: it uses the state-of-the-art MPCC controller for path tracking and motion replanning [5], but without torque vectoring capabilities. The goal is to evaluate the benefits of torque vectoring in terms of added stability

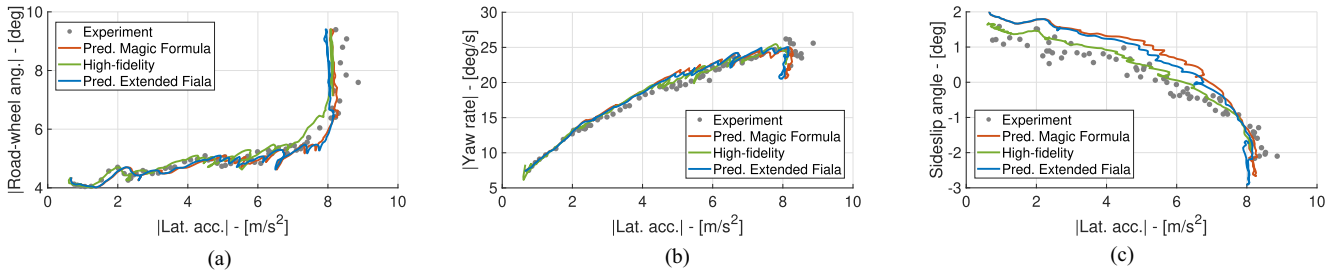

Fig. 5. Experimental model validation of the vehicle characteristics for a skidpad manoeuvre with 40 m radius: (a) understeer gradient, (b) yaw rate and (c) sideslip angle.

and agility during evasive manoeuvrers, specifically for obstacle avoidance at the limit of handling;

- MPCC TV: it uses the same MPCC with torque vectoring as the proposed approach but excludes the collision avoidance prioritization term J_{obs}, see (12), from the cost function. The goal is to demonstrate that the proposed approach provides advantages not only in torque vectoring but also in enhancing overall vehicle safety by prioritising collision avoidance.

All the controllers are evaluated on a double lane change manoeuvre with two obstacles with high and low friction conditions, respectively 1 and 0.5. Additionally, a split μ condition is analysed to assess the controllers' ability to adapt to varying friction levels, thereby preventing excessive sideslip angles while manoeuvring to avoid obstacles. The split μ condition is designed with a high friction coefficient on the right lane ($\mu = 1$) and a low friction coefficient on the left lane ($\mu = 0.5$). A coarse trajectory function of the road distance and the road curvature is provided to the MPCC, simulating the output of a behavioural planner [3], [5]. The desired velocity is assumed constant along the manoeuvre. The controller must track the reference trajectory and perform an online trajectory replanning when the vehicle passes dangerously close to one of the obstacles. This can happen due to different handling limits of the behaviour planner and the path tracking controller, as well as the intervention of the stability controller. The scenario contains two obstacles to demonstrate that the short trajectory replanning around the first obstacle does not interfere with the vehicle's capacity to avoid the subsequent obstacle. The key performance indicators (KPIs) are the V2O and the V2E distances, which must be higher than zero to avoid a collision and preferably higher than 0.5 m to avoid a near-miss collision. A test is considered failed when the vehicle collides with an obstacle or goes outside the road edges.

B. Experimental Model Validation

The computationally efficient vehicle model with the extended Fiala tyre used within the MPCC and the high-fidelity vehicle model with Delft Tyre model are validated with experimental data collected on a proving ground. The test platform was equipped with the conventional Inertial Measurement Unit (IMU), Kistler wheel force transducers, and SKF intelligent bearings installed on each wheel. Additionally, it had a dual antenna GNSS system and a Corrsys-Datron non-contact optical sensor dedicated to measuring the sideslip angle, boasting a measurement accuracy of approximately ± 0.2 deg. Interconnection of all equipment was facilitated through the Controller Area Network (CAN) interface, with the sampling rate configured to operate at 100 Hz.

The accuracy of the models during a 40 m radius skidpad test, a brake-in-turn manoeuvrer with longitudinal and lateral accelerations of 8 m/s^2 and 4 m/s^2 respectively, and a double lane change at 70 km/h are depicted in Figs. 5, 6, 7. In the quasi-steady-state behaviour, both the prediction models and the high-fidelity model demonstrate high accuracy across both linear and nonlinear regions of tyre operation. The only minor discrepancy observed is an overestimation of the sideslip angle by the prediction model, remaining below 1 deg. This overestimation is more pronounced when the Magic Formula tyre model is used, particularly when the absolute value of lateral acceleration exceeds 4 m/s^2. The high-fidelity model exhibits the highest alignment with experimental data during the brake-in-turn manoeuvrer. The prediction model based on the extended Fiala tyre model also achieves high accuracy in predicting yaw rate and vehicle sideslip angle, albeit with a slight overestimation of lateral acceleration. In contrast, the prediction model using the Magic Formula tends to overestimate lateral acceleration and shows a differing trend, underestimating the vehicle's yaw rate during combined longitudinal and lateral forces due to a greater mismatch in the tyre model under such conditions. Given that torque vectoring inputs increase the duration of coupled longitudinal and lateral forces, these results emphasize the importance of the proposed extended Fiala tyre model. Regarding transient vehicle behaviour, all models can capture even the lateral acceleration and the yaw rate peaks recorded with the experimental vehicle. The most significant difference is noticeable in Fig. 7(c), which shows that the high-fidelity model overestimates the measured vehicle sideslip angle at most 0.5 deg, while the prediction model based on the Magic Formula slightly underestimates the peaks of the sideslip angle by a similar margin. However, this minor discrepancy does not interfere with vehicle model validation. The superior accuracy of the prediction model based on the proposed extended Fiala tyre model, compared to the one based on the Magic Formula, underscores the importance of the proposed tyre model. Additionally, it validates the design choice to neglect wheel dynamics in the prediction model, which facilitates increased discretisation time and reduces the computational time of the MPCC, making the real-time implementation feasible on an embedded platform.

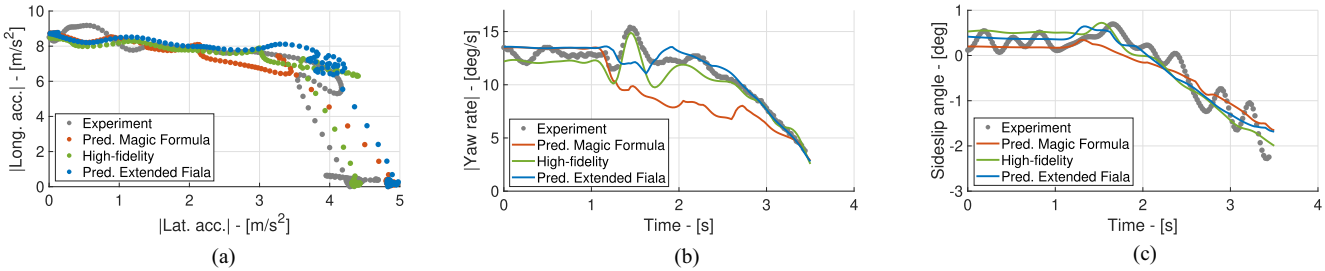

Fig. 6. Experimental model validation of the vehicle characteristics for a brake-in-turn manoeuvre with a $|8|\ m/s^2$ longitudinal and $|4|\ m/s^2$ lateral acceleration: (a) G-G diagram, (b) yaw rate and (c) sideslip angle.

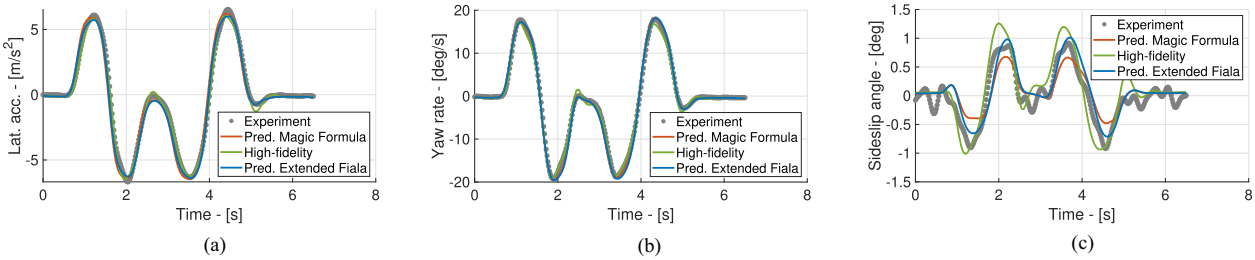

Fig. 7. Experimental model validation of the vehicle characteristics for a double lane change at 70 km/h: (a) lateral acceleration, (b) yaw rate and (c) sideslip angle.

C. Robustness and Sensitivity Analysis Setup

The collision avoidance performance and robustness of the proposed controller are evaluated by considering variations in vehicle parameters and perception inaccuracies. Two different Monte Carlo analyses are conducted to simplify the evaluation of the results, focusing on a double lane change manoeuvre with two obstacles and high friction conditions ($\mu = 1$). The first only assesses the performance by altering the vehicle and tyre parameters, and the second evaluates the effects of obstacle and vehicle localisation inaccuracies. The first Monte Carlo analysis considers the variation of the additional mass (Δm) and corresponding moment of inertia (I_{zz}), electric motor time delay (τ_{em}), and the scaling factors of the front and rear cornering stiffness (Ky_F, Ky_R), lateral peak friction coefficients (μ_{y_F}, μ_{y_R}), longitudinal stiffness shape factors (Kx_F, Kx_R) and tyre relaxation lengths of the vehicle plant (Rel), leaving the vehicle prediction model unchanged. The additional mass variation simulates the change in the vehicle mass due to different amounts of fuel, number of passengers and pieces of luggage. Thus, the nominal additional mass correspondent to 160 kg is varied by $\pm 10\,\%$ of the total vehicle mass according to a Gaussian distribution [15], and its changes are associated with the corresponding variation of I_{zz}. The Δm distribution is visible in Fig. 8(a), and the same approach is used for all the parameters varied according to a Gaussian distribution. A variation of $\pm 15\,\%$ is associated with the electric motor delay, and it simulates the effect of different load conditions, power supply and environmental factors [34]. The tyre cornering stiffnesses, lateral peak friction coefficients, longitudinal stiffness shape factors and tyre relaxation lengths of the vehicle are modified by $\pm 15\,\%$ over their nominal value to simulate the effect of tyre

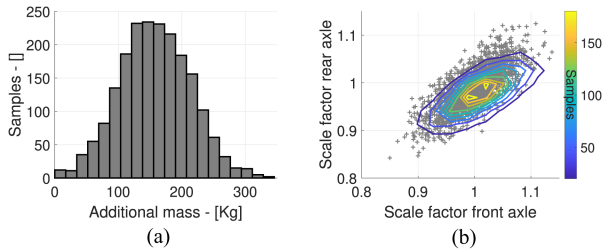

Fig. 8. Gaussian distribution of additional mass Δm (a); normal multivariate distribution of the scaling factors for the cornering stiffness, lateral peak friction coefficients, and longitudinal stiffness shape factors (b).

wear, temperature variations, suspension kinematics, bushing wear and other effects [15], [35]. Considering that tyre wear is not always homogeneous in the four wheels, and that the wear in the suspension bushings can affect the characteristics of the front and rear axles differently [35], the parameters variations of the front and rear axles are varied according to a multivariate normal distribution, see Fig. 8(b). This can model the different front and rear axle variations, but it avoids the unrealistic scenario of a simultaneous increased front cornering stiffness equal to $+15\,\%$ and a $-15\,\%$ reduction in the rear axle cornering stiffness. A similar concept is applied for scaling the μ_{y_F}, μ_{y_R} and Kx_F, Kx_R. Specifically, the prediction model can accommodate a maximum estimation error of $\pm 15\,\%$ for the friction coefficient, distributed according to a multivariate normal distribution, as depicted in Fig. 8(b). The same variation is considered for the front and rear axles regarding the relaxation length. The first Monte Carlo analysis consists of 11000 different simulations generated by a random combination of the varied parameters.

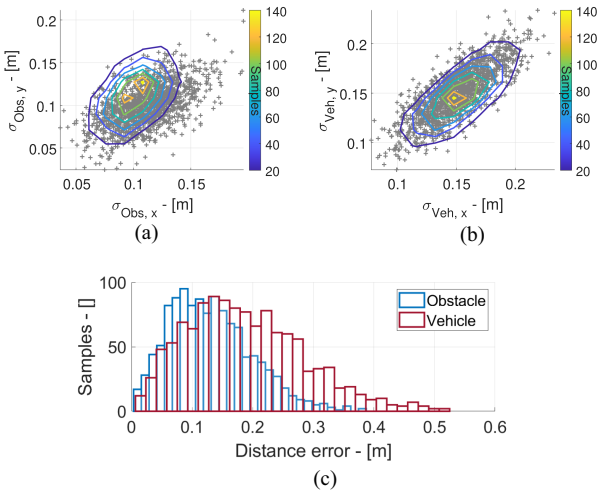

Fig. 9. Multivariate distribution of the standard deviations for lateral and longitudinal errors of obstacle (a) and vehicle (b) localisation; c) distributions of the vehicle and obstacle localisation distance errors generated by the nominal standard deviations.

The second Monte Carlo analysis considers the variation of obstacle localisation error in the longitudinal ($\sigma_{Obs,X}$) and lateral direction ($\sigma_{Obs,Y}$) [36], [37], vehicle localisation error in the longitudinal ($\sigma_{Veh,X}$) and lateral direction ($\sigma_{Veh,X}$) [38], [39] and the percentage of false negative obstacle detections [40]. The obstacle localisation inaccuracies in X and Y directions are modelled as random Gaussian noises in which the standard deviations are varied according to a multivariate normal distribution, see Fig. 9(a). The longitudinal and lateral inaccuracies are not always considered equal because the performance of the obstacle detection algorithm is influenced by the obstacle aspect ratio bias and camera perspective, which can influence in which direction the perception algorithm is more accurate [36]. Fig. 9(c) shows that the most probable standard deviation combination creates a mean distance error equal to 0.13 m for vehicle obstacle localisation, corresponding to the mean average translation error in vehicle detection for the leaderboard works using the nuScenes dataset [41]. The same approach is applied to vehicle localisation which errors in the longitudinal and lateral directions are treated as random Gaussian noises. The noises are varied according to a multivariate normal distribution; see Fig. 9(b). In this situation, the nominal standard deviations create a mean distance error equal to 0.19 m, see Fig. 9(c). The mean value is chosen comparing the performance of different localisation techniques for automated vehicles [42]. Furthermore, the analysis considers the percentage of false negatives modelled through the parameter (λ) of a Poisson distribution, which defines the number of times a random event occurs given a period. It is varied according to a Gaussian distribution with a mean equal to 0.5 and a standard deviation of 0.15. Thus, it corresponds to a probability equal to 16.3 % of having a single false negative during the simulation, 1.7 % of two and 0.2 % of three, corresponding to the performance of the leaderboard works [41]. It is essential to specify that we only model the probability that this event occurs, but where and for how many times it happens is not regulated in the simulation scenario, but it depends on the Poisson distribution. This Monte Carlo analysis consists of 3000 simulations generated by a random combination of the varied parameters. The lower number of simulations compared to the first Monte Carlo analysis is due to the lower number of assessed parameters.

The controller performance is evaluated by computing the Collision Rate (CR), defined as the percentage of simulations in which the vehicle collides with an obstacle or goes out from the road edges. This is measured through the minimum distance between the V2O and V2E, represented by the symbol (mVD). Furthermore, the robustness is evaluated through the Near Miss Rate (NMR), which measures the percentage of simulations in which the vehicle has a *mVD* lower than 0.5 m.

The mVD is also used to perform a sensitivity analysis and mathematically evaluate the standing of which vehicle parameters and perception inaccuracies influence the controller performance most. The proposed sensitivity analysis is based on the PAWN approach [43], and it computes the density-based sensitivity (SI) indices. The PAWN approach assesses the impact of input variables, e.g. vehicle parameters, on the cumulative probability distribution of the output, e.g. mVD, considering the entire distribution rather than just specific moments. Thus, it is less sensitive to skewed or multi-modal distribution than the classical Variance-based sensitivity analysis [44]. The SI indices are dimensionless absolute measures ranging between zero and one. Thus, the non-influential inputs will have a value of zero, and, vice versa, the most influential ones will have a value closer to one.

VI. Results

This section is split into three subsections. Section VI-A demonstrates the improved performance of the proposed MPCC over the baselines in high and low friction conditions with the high-fidelity model based on nominal parameters. Section VI-B proves the robustness of the proposed approach to varying vehicle parameters and perception inaccuracies in the high-fidelity vehicle model. Section VI-C presents the sensitivity analysis results aimed at evaluating the parameters that most significantly influence the controller's performance.

A. Controller Performance

Fig. 10(a) shows the trajectories of the high-fidelity vehicle model with nominal parameters attained by the three different controllers. The proposed MPCC TV+CA is the only controller to drive through the double lane change manoeuvre without colliding with either of the two obstacles. The MPCC TV is unaware of the obstacles' location, so its path tracking and vehicle stability objectives lead the vehicle to collide with the first obstacle located at 99 m. On the other hand, the MPCC CA can successfully avoid the first obstacle, replanning the initial trajectory in a very similar way to the MPCC TV+CA. However, it cannot avoid a collision with the second obstacle due to a loss of stability despite harsh braking from $\sim$ 105 m to $\sim$ 115 m. Vice versa, the MPCC TV+CA stabilises the vehicle between 100 m and 120 m, reducing the vehicle sideslip angle from a peak higher than 15 deg to a peak equal to 7.5 deg. This is

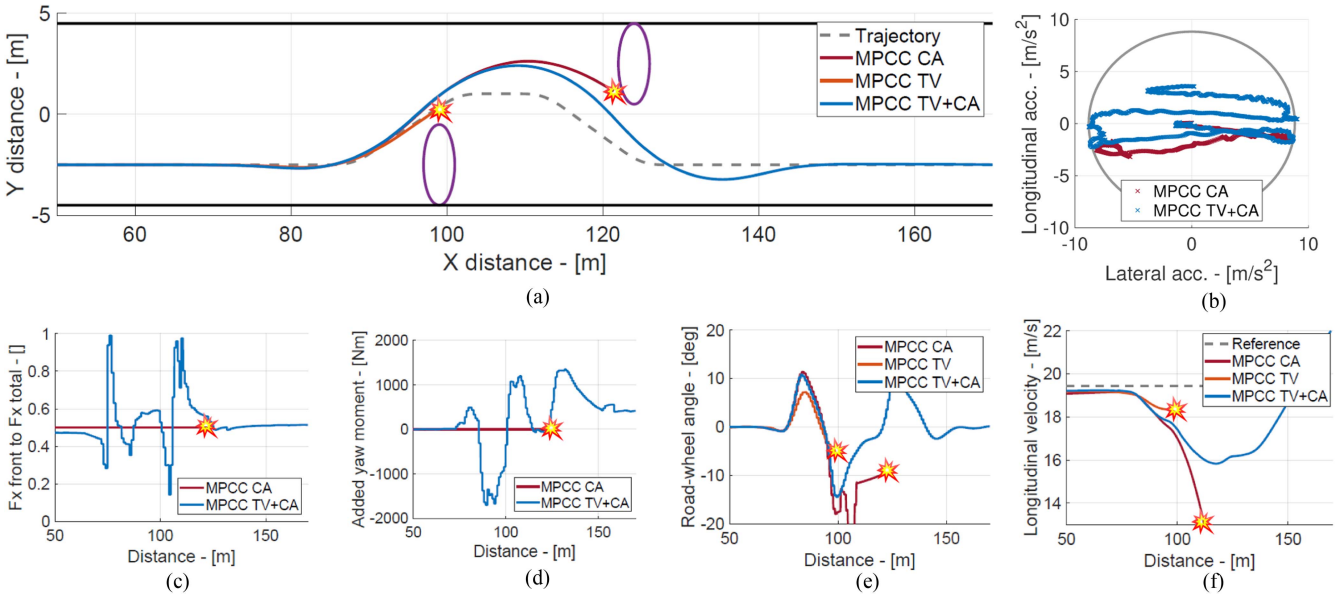

Fig. 10. States and control inputs of the controllers in a double lane change manoeuvre with high friction conditions ($\mu = 1$).

possible thanks to the extra yaw moment, up to ~ 2000 Nm, at the vehicle CoG generated by torque vectoring. Furthermore, it is relevant to notice that thanks to the lower sideslip angle, the vehicle controller MPCC TV+CA can drive through the double lane change at a higher speed than the MPCC CA, without performing any harsh braking after avoiding the first obstacle. Fig. 10(f) shows that the minimum speed of the vehicle driven by the MPCC TV+CA is 16 $\mathrm{m/s}$, while the MPCC CA cannot avoid the second obstacle despite reducing the speed to 13 $\mathrm{m/s}$. The MPCC TV+CA also optimises the front and rear longitudinal force repartition (Fig. 10(c)). The controller moves the brake repartition to the front axle during the hard braking at 90 m. However, the front-rear ratio is restored to 50 $\%$ or even moved to the rear axle, when the vehicle enters the corner, and the front axle has a high road wheel angle (Fig. 10(e)). It is relevant to notice that in both the front and rear axle, the added yaw moment generated by the torque vectoring is substantial in magnitude only during the manoeuvre and at its exit to stabilise the vehicle. On the contrary, the added inequality constraints prevent the MPCC TV+CA from using torque vectoring when the vehicle is driving straight. Regarding the road wheel angle computed by the MPCC CA, it is visible how it already exceeds the constraints at ~ 120 m because the controller cannot converge to an optimal solution. Fig. 10(b) shows that both MPCC controllers with CA capabilities reach the maximum lateral acceleration, which can be generated with the available road friction coefficient. On the contrary, the maximum braking capability is not fully exploited by any controller. This work demonstrates that TV can be integrated into an MPCC with CA avoidance prioritisation and that TV is essential to stabilise the vehicle while avoiding obstacles at the limit of handling. However, the strong coupling between longitudinal and lateral dynamics brings complexity to the MPCC. For this reason, it was essential to improve the accuracy of the prediction model, e.g. including an extended version of the Fiala tyre model.

The proposed controller and the two baselines are also tested in a double lane change manoeuvre with a low friction condition ($\mu = 0.5$) and a 55 $\mathrm{km/h}$ desired initial velocity, corresponding to a heavy rain scenario. Fig. 11(a) shows the three vehicle trajectories, and it is visible how only the newly developed controller can successfully avoid the two obstacles. This further proves the robustness of the proposed controller to different friction conditions. Fig. 11(b) shows how this is achieved while the proposed controller drives the vehicle at the handling limits. To evaluate the controllers' capacity to react to a sudden change in the friction coefficient, we tested the proposed controllers and baselines during a double lane change manoeuvrer under a split μ condition with a desired initial velocity of 55 $\mathrm{km/h}$. This manoeuvrer featured a high-friction surface on the right lane ($\mu = 1$) and a low-friction surface on the left lane ($\mu = 0.5$), as shown in Fig. 12(a). An analysis of the trajectories, shown in Fig. 12(a), indicates that only the proposed controller and the baseline MPCC TV successfully avoided the two obstacles, guiding the vehicle at the limit of handling (see Fig. 12(b)). However, while the baseline MPCC TV approaches the unsafe area near the first obstacle, generating a near-miss event, the proposed approach maintains a safer distance, highlighting the importance of collision avoidance prioritisation. The baseline without collision avoidance prioritization successfully navigates around the first obstacle but fails to avoid the second one due to the sudden drop in road friction. The friction drop, together with the saturation of the steering actuator, leads to an instability which can only be mitigated by controllers that incorporate torque vectoring. The additional yaw moment applied at the vehicle's centre of gravity (Fig. 12(d)) stabilizes the vehicle during the manoeuvrer, allowing it to avoid obstacles effectively. Conversely, the MPCC CA attempts to manage the sudden change in friction primarily through adjustments in the road-wheel angle (Fig. 12(c)) and additional braking force. A particularly notable aspect is the comparison of the additional

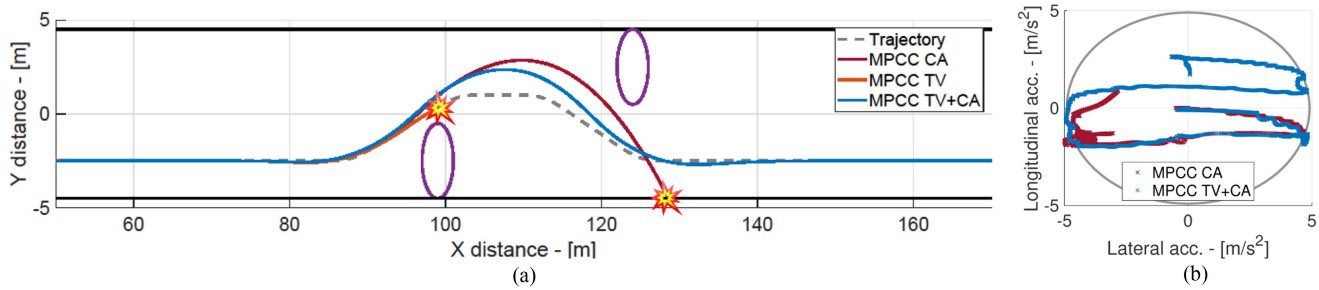

Fig. 11. Vehicle trajectories and G-G diagram in a double lane change manoeuvre with low friction conditions ($\mu = 0.5$).

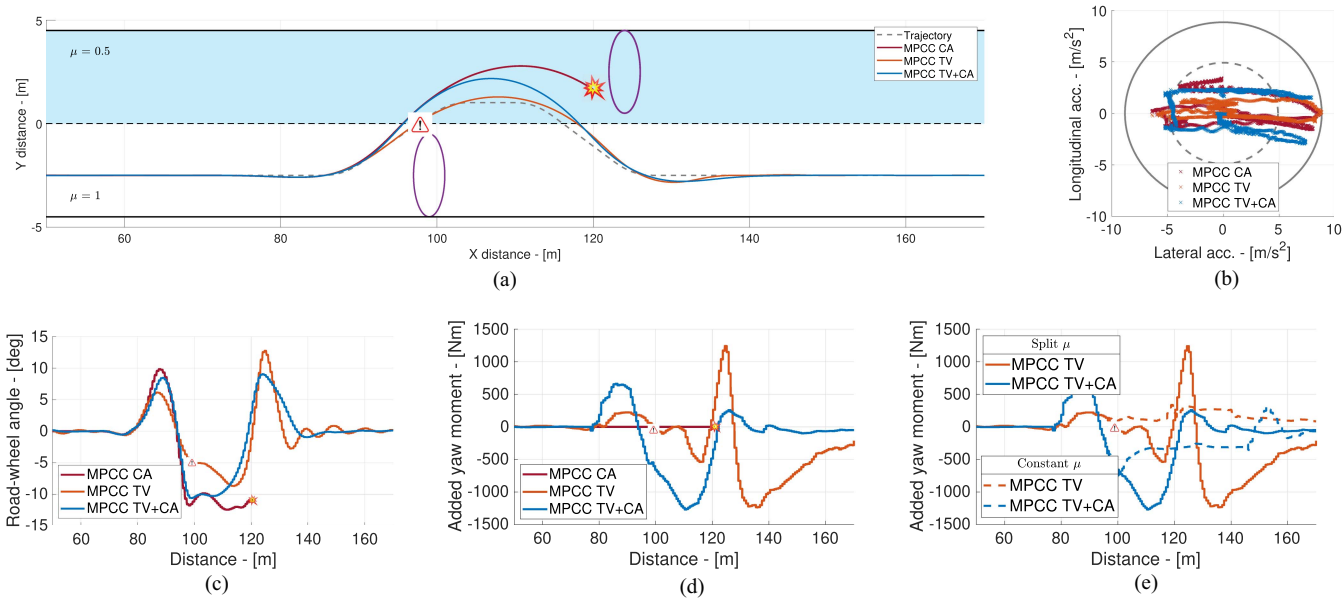

Fig. 12. States and control inputs of the controllers in a double lane change manoeuvre with split μ conditions. The white area has $\mu = 1$, and the light blue area has $\mu = 0.5$.

yaw moment generated by controllers with torque vectoring in the split μ condition versus scenarios with a constant friction coefficient. Fig. 12(e) demonstrates that both controllers with torque vectoring generate additional yaw moments to stabilize the vehicle under the split μ condition, which was unnecessary during the high-friction scenario. This confirms the ability of the proposed controllers to effectively react to sudden changes in the tyre-road friction condition.

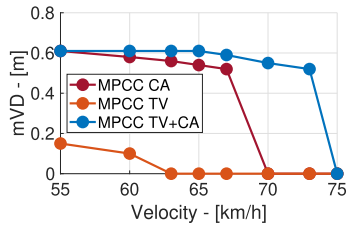

Fig. 13. Analysis of the mVD at the variation of desired initial vehicle velocity in a double lane change.

B. Robustness Analysis

The performance of all the controllers is also evaluated in the same double lane change with high friction conditions ($\mu = 1$), varying the initial and desired vehicle velocities to determine the point at which each controller begins to fail. Fig. 13 shows that the proposed controller effectively avoids the obstacles in the simulated scenario with velocities up to 73 km/h, a 7.5 % improvement over the MPCC CA. In contrast, the MPCC TV successfully executes the manoeuvre only at velocities up to 60 km/h. This analysis further highlights the advantages of incorporating collision avoidance prioritisation and torque vectoring.

The robustness of the proposed controller MPCC TV+CA and the baseline MPCC CA, as explained in Section V-B, are compared at varying velocities in Fig. 14. The controller without collision avoidance is not analysed in this section because it already shows a low performance in nominal conditions; see Fig. 13. Both the analysed controllers show an exponential growth of the collision rate with the increase of vehicle velocity; see Fig. 14(a). However, the proposed controller is substantially more robust to vehicle parameter variations for velocities higher than 60 km/h. On the other hand, they show a similar CR, corresponding to ~ 5 % for lower velocities because the vehicle

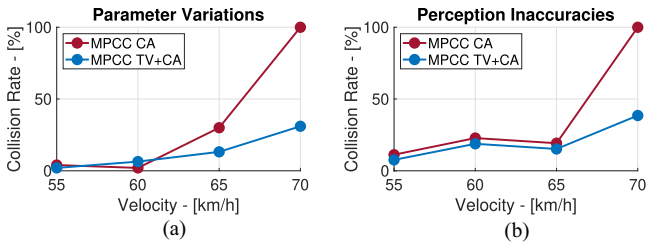

Fig. 14. Robustness evaluation to vehicle parameters (a) and perception inaccuracies (b) of the analysed controllers at varying velocities.

TABLE IV
MONTE CARLO ANALYSIS RESULTS RELATED TO VEHICLE PARAMETER VARIATIONS AND PERCEPTION INACCURACIES FOR THE PROPOSED CONTROLLER

Configuration	Collision Rate [%]	Near Miss Rate [%]
Parameter Variations	31.20	34.80
Perception Inaccuracies	38.50	49.50

TABLE V
DIFFERENT COLLISION PATTERNS OBSERVED IN THE MONTE CARLO ANALYSIS FOR THE PROPOSED CONTROLLER

	Obstacle 1 [%]		Obstacle 2 [%]		Edge Left [%]		Edge Right [%]	
	CR	NMR	CR	NMR	CR	NMR	CR	NMR
Parameter Variations	3.21	36.49	22.76	38.51	23.72	26.72	50.32	51.72
Perception Inaccuracies	54.67	94.48	1.38	4.17	4.67	9.82	39.27	30.55

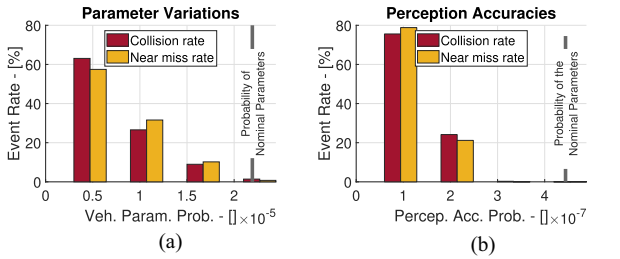

Fig. 15. Collision and Near Miss Rates change to the probabilities variation of parameter configurations for parameter variations (a) and perception inaccuracies (b).

behaves less nonlinearly and the scenario allows a higher margin of error. Thus, the controller task is simplified, and both can achieve an optimum level of robustness. Vice versa, vehicle dynamics become highly nonlinear at high velocities, and the scenario becomes more challenging. In this situation, both controllers reduce their robustness. However, the MPCC TV+CA can achieve adequate robustness thanks to the extra added yaw moment, which increases the vehicle responsiveness.

Fig. 14(b) shows the controllers' robustness to vehicle perception inaccuracies at different velocities. Similar to the above case, the proposed approach shows a higher robustness than the controller without torque vectoring. However, it is noticeable that the MPCC TV+CA and the MPCC CA show similar robustness to velocities up to 65 $\mathrm{km/h}$. A possible explanation is that the most significant cause of failure up to this velocity is the obstacle lateral error noise, which leads to an impossible scenario for both MPCCs. Thus, the major difference between MPCC TV+CA and MPCC TV for perception inaccuracies robustness happens at a velocity equal to 70 $\mathrm{km/h}$, where the torque vectoring allows a higher accuracy even in nominal conditions.

Considering the scope of the paper, which is to assess the performance of the proposed controller at the limit of handling, we will focus on the robustness analysis of the MPCC TV+CA during the double lane change at 70 $\mathrm{km/h}$. Table IV presents the results of the controller robustness analysis against variations in vehicle parameters. The proposed MPCC TV+CA is the only one with a CR lower than 100 % among the controllers evaluated. Although the vehicle parameters variations impact the proposed controller's performance, a CR equal to 31 % and an NMR of 35 % demonstrate the MPCC TV+CA robustness. The slight difference between NMR and CR suggests that the controller can avoid obstacles only a few times when it enters the danger zone. However, the vehicle collides with a velocity on average 29 % lower than its reference velocity. Thus, it can still mitigate the consequences of collisions. Particularly interesting are the collision patterns at the variation of the vehicle parameters; see Table V. Approximately 50 % of collisions occur due to the vehicle driving off-road on the right side. This indicates that the controller can successfully drive the vehicle around the obstacles, but it compromises its ability to rejoin the original trajectory. This behaviour may stem from increased model mismatch caused by parameter variations, impacting the controller's efficacy. Further proof is the 23 % of collision with the second obstacle, which indicates how the vehicle can safely avoid the first collision but cannot avoid the second one. Although the collision rate is at 31 %, as depicted in Fig. 15(a), it is evident that the trend in collision rates is exponentially decreasing with the occurrence of vehicle parameter configurations with higher probability. This observation underscores the robustness of the proposed controller to vehicle parameter variations, as it highlights that the 90 % of collisions occurs for configurations where parameters are situated in the tails of the Gaussian distribution, so less probable configurations in a real-life scenario. The configurations with the highest probability have only $\sim$ 1 % of collisions.

Table IV also presents the results of the controller robustness to perception inaccuracies. The proposed MPCC TV+CA demonstrates robustness comparable to that under vehicle parameter variations, achieving a CR of 38.5 % and an NMR of 49.5 %. This underscores the robustness of the proposed approach not only against vehicle parameter variations but also against uncertainties in vehicle and obstacle localisation. In contrast to the previous scenario, when the controller fails, it leaves the roadway only 44 % of the time, see Table V. Particularly noteworthy is that in 55 % of collision cases, the first obstacle encountered results in a collision. This suggests that the MPCC TV+CA, influenced by uncertainties in the vehicle and obstacle localisation, can fail to promptly replan its trajectory around obstacles. In comparison, under vehicle parameter variations, the MPCC TV+CA primarily fails after successfully avoiding the first and second obstacles. An explanation for this could be the increased error in obstacle localisation, which causes

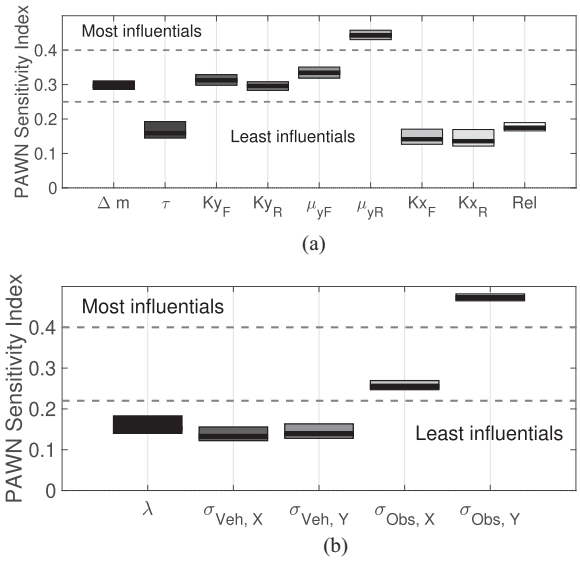

Fig. 16. Sensitivity analysis results for vehicle parameter variations (a) and vehicle perception inaccuracies (b).

the MPCC TV+CA to be unaware of its proximity to obstacles, leading to hazardous situations. Furthermore, erroneous obstacle localisation can mislead the MPCC TV+CA into believing that the road ahead is obstructed, preventing the vehicle from passing safely with adequate distance.

Fig. 15(b) shows the trend in collision and near miss rates as the probability of perception inaccuracies decreases. As expected, the 75 % of collisions happens when the proposed controller is affected by the lowest probability of perception accuracies. Once again, the exponential decrease in the number of collisions and near-miss rate events with the increase of perception accuracy probability highlights the robustness of the proposed controller.

C. Sensitivity Analysis

Fig. 16(a) shows the SI indices for the PAWN sensitivity analysis evaluating the vehicle parameter variations. The box plot area represents the uncertainty of these indices, which has been minimised due to the extensive number of simulations conducted. It is visible that the nine analysed parameters can be split into three influential groups. The most influential group consists of only one parameter: the lateral peak friction coefficient for the rear axle (μ_{y_R}). This suggests that μ_{y_R} influences the performance of the proposed controller the most, which can be explained by the fact that a decrease in μ_{y_R} can lead the vehicle to an oversteer behaviour, which is particularly difficult to control and stabilise even for a human driver [45]. The second group is composed of Δm, the front and rear axle cornering stiffness (Ky_F and Ky_R) and the front axle lateral peak friction coefficient. Once again, the parameters Ky_F, Ky_R and μ_{y_F} can strongly vary the vehicle behaviour, changing it from understeer to oversteer and vice versa. A similar conclusion can also be stated for Δm because it is not placed in the vehicle CoG, so it moves the CoG location. The least influential parameters are the front and rear axle longitudinal stiffness shape factors (Kx_F and Kx_R), the tyre relaxation length (Rel) and the electric motor delay (τ). The relative non-influential effect on the proposed controller performance can be explained by the fact that the analysis scenario involves primarily the vehicle lateral dynamics and not the longitudinal one, which is most affected by the Kx_F and Kx_R. The analysis of the effect of Rel and τ suggests that the controller can deal adequately with an additional delay. A proof is that a similar MPCC controller has also successfully been implemented for a vehicle with hydraulic brakes [5], which have even slower dynamics. Fig. 16(b) shows the SI indices for vehicle perception uncertainties. The analysis reveals that the five examined parameters can be categorised into three distinct levels of influence. The most influential one consists of the lateral obstacle localisation ($\sigma_{Obs,Y}$) error which strongly limits the controller's capacity to avoid obstacles. A possible explanation is that the increased $\sigma_{Obs,Y}$ can lead to an impossible scenario for the MPCC. For instance, a further step of the first or second obstacle towards the road centre can make collision avoidance unfeasible. The second group consists of $\sigma_{Obs,X}$. Interestingly, controller failure can occur not only due to the magnitude of noise but, more critically, due to the direction and timing of misleading obstacle localisation. This means that vehicle obstacle localisation errors are the most influencing factors for controller performance, and they must be carefully considered during the controller design. The third group include the vehicle localisation errors and the false negative probability. It is expected that $\sigma_{Veh,X}$, $\sigma_{Veh,Y}$ could have a similar effect on the MPCC performance than $\sigma_{Obs,X}$ and $\sigma_{Obs,Y}$. However, the MPCC feedback on the vehicle localisation can partially compensate for their effect. The relatively lower influence of the false negative percentage (coefficient λ) can be attributed to its probabilistic nature. Since we cannot control when a false negative occurs within a scenario, it may happen when the vehicle is too far from the obstacle to be influenced by it. However, controlling the timing of false negatives is unrealistic and, thus, has not been analysed in this study.

VII. Conclusion

This paper presents a novel approach to vehicle obstacle avoidance. It is based on a nonlinear Model Predictive Contouring Control, which employs torque vectoring capabilities to stabilise the vehicle, performing evasive manoeuvres at the limit of handling. The proposed controller with torque vectoring and collision avoidance successfully avoids the two obstacles in the Double Lane Change manoeuvre with high and low friction conditions, and it has proven to work on a rapid prototyping platform in real-time with an average solving time of 38.9 ms. The first baseline controller without collision avoidance collides with the first obstacle due to its lack of motion replanning capability. The second baseline controller without torque vectoring cannot stabilise the vehicle after avoiding the first obstacle, and it collides with the second one. The proposed controller produces an extra yaw moment up to $\sim$ 2000 Nm in magnitude, increasing the vehicle's lateral agility to avoid the obstacles and reduce the vehicle sideslip angle peak down to 7.5 deg rather

than the 16 deg for the second baseline controller without torque vectoring. However, the proposed controller requires a more accurate prediction model, so an extended Fiala tyre model has been developed to describe the tyre behaviour in combined slip conditions. Using extended Monte Carlo analyses, the proposed controller shows robustness to vehicle parameter variations and perception inaccuracies with a collision rate of respectively 31.20 % and 38.50 %. As further proof, the percentage of crashes occurring with simulated values near the nominal vehicle parameters and the most probable vehicle perception inaccuracies is below 1.5 %. Furthermore, the results of sensitivity analysis are statistically assessed to evaluate the sensitivity indices to each analysed parameter. The lateral peak friction coefficient of the rear axle and the obstacle localisation error in the lateral direction have a higher effect on the controller performance. Future works involve the experimental validation of the proposed controller and the enhancement of the algorithm to better deal with the most influential parameters.

REFERENCES

[1] N. Chowdhri, L. Ferranti, F. Iribarren, and B. Shyrokau, "Integrated nonlinear model predictive control for automated driving," *Control Eng. Pract.*, vol. 106, 2021, Art. no. 104654.

[2] J. K. Subosits and J. C. Gerdes, "Impacts of model fidelity on trajectory optimization for autonomous vehicles in extreme maneuvers," *IEEE Trans. Intell. Vehicles*, vol. 6, no. 3, pp. 546–558, Sep. 2021.

[3] R. Hajiloo, M. Abroshan, A. Khajepour, A. Kasaiezadeh, and S.-K. Chen, "Integrated steering and differential braking for emergency collision avoidance in autonomous vehicles," *IEEE Trans. Intell. Transp. Syst.*, vol. 22, no. 5, pp. 3167–3178, May 2021.

[4] S. Teng et al., "Motion planning for autonomous driving: The state of the art and future perspectives," *IEEE Trans. Intell. Veh.*, vol. 8, no. 6, pp. 3692–3711, Jun. 2023.

[5] A. Bertipaglia, M. Alirezaei, R. Happee, and B. Shyrokau, "Model predictive contouring control for vehicle obstacle avoidance at the limit of handling," in *Proc. Adv. Dyn. Vehicles Roads Tracks III*, 2024, pp. 132–142.

[6] M. Brown and J. C. Gerdes, "Coordinating tire forces to avoid obstacles using nonlinear model predictive control," *IEEE Trans. Intell. Vehicles*, vol. 5, no. 1, pp. 21–31, Mar. 2020.

[7] D. Lenssen, A. Bertipaglia, F. Santafe, and B. Shyrokau, "Combined path following and vehicle stability control using model predictive control," Society of Automobile Engineers, Pennsylvania, PA, USA, Technical Paper, Tech. Rep. 2023-01-0645, 2023.

[8] E. Hashemi and A. Khajepour, "Integrated path-tracking and combined-slip force controls of autonomous ground vehicles with safe constraints adaptation," *IEEE Trans. Intell. Veh.*, vol. 9, no. 3, pp. 4265–4274, Mar. 2024.

[9] W. Degel, S. Lupberger, D. Odenthal, and N. Bajcinca, "Scalable slip control with torque vectoring including input-to-state stability analysis," *IEEE Trans. Control Syst. Technol.*, vol. 31, no. 3, pp. 1250–1265, May 2023.

[10] L. De Novellis, A. Sorniotti, P. Gruber, and A. Pennycott, "Comparison of feedback control techniques for torque-vectoring control of fully electric vehicles," *IEEE Trans. Veh. Technol.*, vol. 63, no. 8, pp. 3612–3623, Oct. 2014.

[11] P. K. Wong and D. Ao, "A novel event-triggered torque vectoring control for improving lateral stability and communication resource consumption of electric vehicles," *IEEE Trans. Intell. Vehicles*, vol. 9, no. 1, pp. 2046–2060, Jan. 2024.

[12] A. Bertipaglia et al., "Model predictive contouring control for vehicle obstacle avoidance at the limit of handling using torque vectoring," in *Proc. Int. Conf. Adv. Intell. Mechatron.*, 2024, pp. 1468–1475.

[13] Y. Ren, L. Zheng, and A. Khajepour, "Integrated model predictive and torque vectoring control for path tracking of 4-wheel-driven autonomous vehicles," *IET Intell. Transport Syst.*, vol. 13, no. 1, pp. 98–107, 2019.

[14] C. Chatzikomis, A. Sorniotti, P. Gruber, M. Zanchetta, D. Willans, and B. Balcombe, "Comparison of path tracking and torque-vectoring controllers for autonomous electric vehicles," *IEEE Trans. Intell. Vehicles*, vol. 3, no. 4, pp. 559–570, Dec. 2018.

[15] P. Stano et al., "Enhanced active safety through integrated autonomous drifting and direct yaw moment control via nonlinear model predictive control," *IEEE Trans. Intell. Veh.*, vol. 9, no. 2, pp. 4172–4190, Feb. 2024.

[16] Y. Yu, W. Ji, R. Li, A. Lu, and G. Tian, "Vehicle motion control beyond and within the stability limits for 4wd electric vehicles," *IEEE Trans. Intell. Veh.*, vol. 9, no. 1, pp. 2348–2363, Jan. 2024.

[17] A. Liniger, A. Domahidi, and M. Morari, "Optimization-based autonomous racing of 1: 43 scale RC cars," *Optimal Control Appl. Methods*, vol. 36, no. 5, pp. 628–647, 2015.

[18] P. Falcone, F. Borrelli, H. E. Tseng, J. Asgari, and D. Hrovat, "A Hierarchical model predictive control framework for autonomous ground vehicles," in *Proc. Amer. Control Conf.*, 2008, pp. 3719–3724.

[19] Y. Gao, A. Gray, A. Carvalho, E. Tseng, and F. Borrelli, "Robust nonlinear predictive control for semiautonomous ground vehicles," in *Proc. Amer. Control Conf.*, 2014, pp. 4913–4918.

[20] V. Mazzilli et al., "Integrated chassis control: Classification, analysis and future trends," *Annu. Rev. Control*, vol. 51, pp. 172–205, 2021.

[21] D. Kasinathan, A. Kasaiezadeh, A. Wong, A. Khajepour, S.-K. Chen, and B. Litkouhi, "An optimal torque vectoring control for vehicle applications via real-time constraints," *IEEE Trans. Veh. Technol.*, vol. 65, no. 6, pp. 4368–4378, Jun. 2016.

[22] Y. Liang, Y. Li, A. Khajepour, and L. Zheng, "Holistic adaptive multi-model predictive control for the path following of 4WID autonomous vehicles," *IEEE Trans. Veh. Technol.*, vol. 70, no. 1, pp. 69–81, Jan. 2021.

[23] T. P. Weber and J. C. Gerdes, "Modeling and control for dynamic drifting trajectories," *IEEE Trans. Intell. Veh.*, vol. 9, no. 2, pp. 3731–3741, Feb. 2024.

[24] V. A. Laurense and J. C. Gerdes, "Long-horizon vehicle motion planning and control through serially cascaded model complexity," *IEEE Trans. Control Syst. Technol.*, vol. 30, no. 1, pp. 166–179, Jan. 2022.

[25] H. Pacejka, *Tire and Vehicle Dynamics*. Amsterdam, The Netherlands: Elsevier, 2005.

[26] A. Bertipaglia, B. Shyrokau, M. Alirezaei, and R. Happee, "A two-stage Bayesian optimisation for automatic tuning of an unscented kalman filter for vehicle sideslip angle estimation," in *Proc. IEEE Intell. Veh. Symp.*, 2022, pp. 670–677.

[27] A. Bertipaglia, D. de Mol, M. Alirezaei, R. Happee, and B. Shyrokau, "Model-based vs data-driven estimation of vehicle sideslip angle and benefits of tyre force measurements," in *Proc. Int. Sympos. Adv. Vehi. Contr.*, Kanagawa, Japan, 2022.

[28] A. Bertipaglia, M. Alirezaei, R. Happee, and B. Shyrokau, "An unscented kalman filter-informed neural network for vehicle sideslip angle estimation," *IEEE Trans. Veh. Technol.*, vol. 73, no. 9, pp. 12731–12746, Sep. 2024.

[29] A. Zanelli, A. Domahidi, J. Jerez, and M. Morari, "FORCES NLP: An efficient implementation of interior-point methods for multistage nonlinear nonconvex programs," *Int. J. Control*, vol. 93, pp. 13–29, 2017.

[30] C. Yu, Y. Zheng, B. Shyrokau, and V. Ivanov, "MPC-based path following design for automated vehicles with rear wheel steering," in *Proc. IEEE Int. Conf. Mechatron.*, 2021, pp. 1–6.

[31] V. Vidal et al., "On pre-emptive in-wheel motor control for reducing the longitudinal acceleration oscillations caused by road irregularities," *IEEE Trans. Veh. Technol.*, vol. 71, no. 9, pp. 9322–9337, Sep. 2022.

[32] A. Parra, D. Tavernini, P. Gruber, A. Sorniotti, A. Zubizarreta, and J. Pérez, "On nonlinear model predictive control for energy-efficient torque-vectoring," *IEEE Trans. Veh. Technol.*, vol. 70, no. 1, pp. 173–188, Jan. 2021.

[33] A. Scamarcio et al., "Predictive anti-jerk and traction control for V2X connected electric vehicles with central motor and open differential," *IEEE Trans. Veh. Technol.*, vol. 72, no. 6, pp. 7221–7239, Jun. 2023.

[34] D. Savitski, V. Ivanov, B. Shyrokau, J. De Smet, and J. Theunissen, "Experimental study on continuous abs operation in pure regenerative mode for full electric vehicle," *SAE Int. J. Passenger Cars- Mech. Syst.*, vol. 8, no. 2015-01-9109, pp. 364–369, 2015.

[35] C. Lugaro, M. Alirezaei, I. Konstantinou, and A. Behera, "A study on the effect of tire temperature and rolling speed on the vehicle handling response," Society of Automobile Engineers, Pennsylvania, PA, USA, Technical Paper, Tech. Rep. 2020-01-1235, 2020.

[36] Y. Dong et al., "Benchmarking robustness of 3d object detection to common corruptions," in *Proc. IEEE/CVF Conf. Comput. Vis. Pattern Recognit.*, 2023, pp. 1022–1032.

[37] C. Zhang, H. Wang, L. Chen, Y. Li, and Y. Cai, "MixedFusion: An efficient multimodal data fusion framework for 3-D object detection and tracking," *IEEE Trans. Neural Netw. Learn. Syst.*, vol. 36, no. 1, pp. 1842–1856, Jan. 2025.

[38] A. Artuñedo, J. Villagra, J. Godoy, and M. D. d. Castillo, "Motion planning approach considering localization uncertainty," *IEEE Trans. Veh. Technol.*, vol. 69, no. 6, pp. 5983–5994, Jun. 2020.
[39] A. Pfrunder, P. V. K. Borges, A. R. Romero, G. Catt, and A. Elfes, "Real-time autonomous ground vehicle navigation in heterogeneous environments using a 3D LiDAR," in *Proc. IEEE/RSJ Int. Conf. Intell. Robots Syst.*, 2017, pp. 2601–2608.
[40] A. Palffy, E. Pool, S. Baratam, J. F. P. Kooij, and D. M. Gavrila, "Multi-class road user detection with 3+1D radar in the view-of-delft dataset," *IEEE Robot. Automat. Lett.*, vol. 7, no. 2, pp. 4961–4968, Apr. 2022.
[41] H. Caesar et al., "nuScenes: A multimodal dataset for autonomous driving," in *Proc. IEEE/CVF Conf. Comput. Vis. Pattern Recognit.*, 2020, pp. 11621–11631.
[42] Y. Lu, H. Ma, E. Smart, and H. Yu, "Real-time performance-focused localization techniques for autonomous vehicle: A review," *IEEE Trans. Intell. Transp. Syst.*, vol. 23, no. 7, pp. 6082–6100, Jul. 2022.
[43] F. Pianosi and T. Wagener, "Distribution-based sensitivity analysis from a generic input-output sample," *Environ. Modelling Softw.*, vol. 108, pp. 197–207, 2018.
[44] A. Puy, S. L. Piano, and A. Saltelli, "A sensitivity analysis of the pawn sensitivity index," *Environ. Modelling Softw.*, vol. 127, 2020, Art. no. 104679.
[45] M. Alirezaei, S. Jansen, A. Schmeitz, and A. Madhusudhanan, "Collision avoidance system using state dependent Riccati equation technique: An experimental robustness evaluation," in *Proc. Adv. Veh. Control*, 2016, pp. 125–132.

Alberto Bertipaglia (Graduate Student Member, IEEE) received the M.Sc. degree, (cum laude), in automotive engineering from the Politecnico di Torino, Italy, in 2020. He is currently working toward the Ph.D. degree with the Department of Cognitive Robotics,the Delft University of Technology, Delft, The Netherlands. His work is the part of a national research project aiming to develop innovative active vehicle controls to improve vehicle stability and increase the safety of automated vehicles performing evasive manoeuvres.

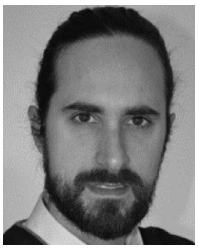

Davide Tavernini received the M.Sc. degree in mechanical engineering, and the Ph.D. degree in dynamics and design of mechanical systems from the University of Padova, Padua, Italy, in 2010 and 2014. During the Ph.D. he was part of the motorcycle dynamics research group. He is a Senior Lecturer in advanced vehicle engineering with the University of Surrey, Guildford, U.K. His research interests include vehicle dynamics modeling, control and state estimation, applied to over-actuated vehicles.

Umberto Montanaro received the M.Sc. degree in computer science engineering, and the Ph.D. degrees in control engineering and mechanical engineering, from the University of Naples Federico II, Naples, Italy, in 2005, 2009, and 2016, respectively. He is currently a Senior Lecturer in control engineering and autonomous systems with the University of Surrey, Guildford, U.K. He is the Director of Surrey team for the Control of Smart Multi-agent systems Operating autonomously and Synergistically. His research interests include adaptive control, and control of piecewise affine, mechatronic, automotive systems and coordination of networked autonomous systems.

Mohsen Alirezaei received the Ph.D. degree in mechanical engineering, robotics and control in 2011, and was a Postdoc Researcher with Delft University of Technology, Delft, The Netherlands in 2012. He was a Senior Scientist with Integrated Vehicle Safety Department, TNO Automotive during 2012–2019, and a part-time Assistant Professor with the Delft University of Technology during 2015–2019. He is currently a Fellow Scientist with Siemens Industry Software and Services, Helmond, The Netherlands, and a part-time Assistant Professor with the Eindhoven University of Technology, The Netherlands. His research interests include the verification and validation of automated and cooperative automated driving and advanced driver assistance systems.

Riender Happee received the Ph.D. degree from Delft University of Technology, The Netherlands, in 1992. During 1992–2007, he investigated road safety and introduced biomechanical human models for impact and comfort with TNO Automotive. Currently, he is a Full Professor with the Delft University of Technology, where he is currently investigates human interaction with automated vehicles, focusing on safety, motion comfort and acceptance.

Aldo Sorniotti (Member, IEEE) received the M.Sc. degree in mechanical engineering and the Ph.D. degree in applied mechanics from the Politecnico di Torino, Turin, Italy, in 2001 and 2005, respectively. He was the Professor and Head of the Centre of Automotive Engineering of the University of Surrey, Guildford, U.K. He is currently a Full Professor in applied mechanics with the Politecnico di Torino, Italy. His research interests include vehicle dynamics control and transmission systems for electric and hybrid electric vehicles.

Barys Shyrokau received the DiplEng degree (cum laude), in mechanical engineering from the Belarusian National Technical University, Minsk, Belarus in in 2004, and a joint Ph.D. degree, in control engineering from Nanyang Technological University, Singapore, and Technical University of Munich, Germany in 2015. He is an Associate Professor with the Delft University of Technology, The Netherlands. His research interests include vehicle dynamics and control, motion comfort, and driving simulator technology. He was the recipient of the Scholarship of IFAC, SAE, FISITA, DAAD, SINGA, ISTVS, and CADLM.